Dynamic heterogeneity and non-Gaussian statistics for ganglioside GM1s and acetylcholine receptors on live cell membrane

Wei He[a], Yun Su[b], H. Benjamin Peng[c], and Penger Tong[b,*]
[a]Nano Science and Technology Program, [b]Department of Physics, and [c]Division of Life Science, Hong Kong University of Science and Technology, Clear Water Bay, Kowloon, Hong Kong

ABSTRACT **We have carried out a comparative study of the lateral motion of ganglioside GM1, which is a glycosphingolipid residing on the outer leaflet of the plasma membrane, and acetylcholine receptor (AChR), which is a well-characterized ion channel. Both the lipid molecules and the transmembrane proteins reside on the plasma membranes of live *Xenopus* muscle cells. From a thorough analysis of a large volume of individual molecular trajectories obtained from more than 300 live cells over a wide range of sampling rates and long durations, we find that the GM1s and AChRs share the same dynamic heterogeneity and non-Gaussian statistics. Our measurements with the ATP-depleted cells reveal that the diffusion dynamics of the GM1s and AChRs is uniformly affected by the intracellular ATP level of the living muscle cells, further demonstrating that membrane diffusion is strongly coupled to the dynamics of the underlying cortical actin network, as predicted by the dynamic picket-fence model.**

Monitoring Editor
Patricia Bassereau
Institut Curie

Received: Sep 11, 2019
Revised: Jan 21, 2020
Accepted: Apr 21, 2020

INTRODUCTION

Cell communication with the outside world takes place at the cell membrane, where membrane-bound protein receptors acquire extracellular stimuli and trigger the release of intracellular second messengers through a sequence of tightly regulated protein interactions (Engelman, 2005). Such molecular events require the participating membrane proteins and lipids to be positioned at specific locations and at appropriate times. To ensure that this happens, the plasma membrane remains highly dynamic, allowing molecules to be transported "vertically" through the membrane and to move "laterally" within the membrane. In the original fluid mosaic model (Singer and Nicolson, 1972), the cell membrane was thought of as a quasi–two dimensional (2D) fluid layer with membrane proteins dispersed as individual moving islands. The dynamics of the membrane molecules is thus determined primarily by the viscous damping of the cell membrane and surrounding medium (Saffman and Delbrück, 1975). However, many recent studies have revealed that there are a wide range of structures on the membrane, which give rise to dynamic heterogeneity at the nano- and microscales (Gelles *et al.*, 1988; Jacobson *et al.*, 1995; Munro, 2003; Kusumi *et al.*, 2005; Lingwood and Simons, 2010; Almarza *et al.*, 2014; Fujiwara *et al.*, 2016; Sezgin *et al.*, 2017; Shi *et al.*, 2018; Jacobson *et al.*, 2019).

Although our general view of molecular motion in living cells has evolved with recent discoveries of the slow active remodeling of the cytoskeletal network due to the activity of molecular motors and other nonequilibrium cellular processes (Gowrishankar *et al.*, 2012; Luo *et al.*, 2013; Guo *et al.*, 2014; Parry *et al.*, 2014), as yet we still do not have a quantitative answer as to how and to what extent the active dynamics in the living cell affects the statistics of the protein motion. The lack of a systematic analysis of the protein motion is partially due to the fact that direct measurement of the statistical properties, such as the probability density function (normalized histogram or PDF) $P(\Delta x)$ of the protein's displacement $\Delta x(\tau)$ over a long delay time τ often requires a large volume of individual protein trajectories, which are difficult to obtain from living cells. As a result, most previous studies in this area only measured the mean squared displacement (MSD), $\langle \Delta x^2(\tau) \rangle$, which requires less statistics. It is now

This article was published online ahead of print in MBoC in Press (http://www.molbiolcell.org/cgi/doi/10.1091/mbc.E19-08-0473) on April 29, 2020.

*Address correspondence to: Penger Tong (penger@ust.hk).

Abbreviations used: AChR, acetylecholine receptor; ATP, adenosine triphosphate; CTX, cholera toxin B subunit; DPF model, dynamic picket-fence model; GM1, monosialotetrahexosylganglioside; MSD, mean-squared displacement; PDF, probability density function; QD, quantum dot; SPT, single-particle tracking.

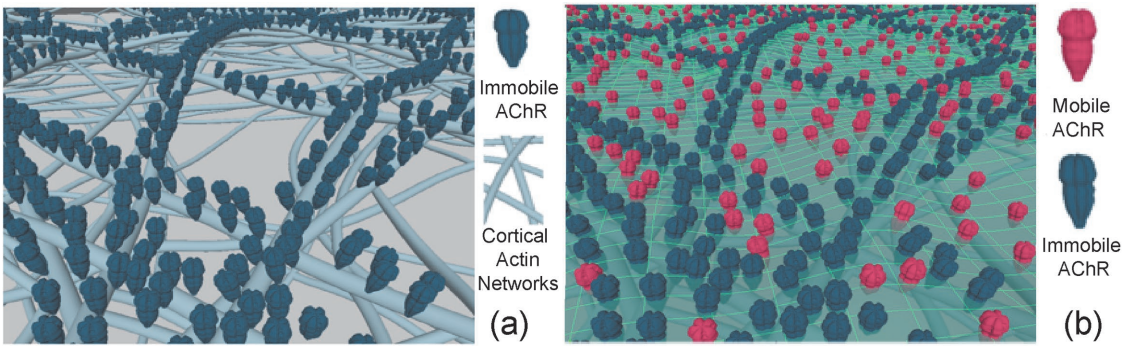

FIGURE 1: Explanation of the dynamic picket-fence model. (a) Cortical actin network with anchored proteins (blue), which form a continuous random network, partitioning the membrane into corrals of different sizes. (b) The motion of mobile proteins (red) is confined to corrals, whose lift time is determined by the slow dynamics of the cortical network. As a result, the diffusion of the mobile proteins is strongly influenced by the size of the corrals, giving rise to a broad distribution of the local diffusion coefficient δ.

generally acknowledged that the MSD fits alone are not sufficient to distinguish between physically different microscopic models for membrane diffusion (Daumas *et al.*, 2003; Höfling and Franosch, 2013).

In a recent experiment (He *et al.*, 2016), we carried out a systematic study of the lateral motion of a transmembrane protein on live muscle cell membrane cultured from *Xenopus* embryos. The protein chosen for the study was acetylcholine receptor (AChR), which is a well-characterized neurotransmitter receptor for the study of neuromuscular junctions (Geng *et al.*, 2009, Zhang and Peng, 2011). The lateral mobility of AChRs plays an essential role in determining the response of the postsynaptic membrane to neurotransmitter stimuli. With the help of photostable fluorescent labeling of the individual AChRs with quantum dots and an advanced single-molecule tracking algorithm, we were able to obtain a significantly large volume of individual AChR trajectories from more than 360 live cells over a wide range of sampling rates (up to 80 frames per second [fps]) and long delay times (up to 200 s).

A central finding of this investigation was that the mobile trajectories of the individual AChRs do not follow the Gaussian statistics for normal Brownian diffusion. Instead, it was found that the measured PDF $P(\Delta x)$ has an exponential tail, which is robust and universal for cells under different conditions. Furthermore, the structurally identical AChRs were found to have very different dynamic behavior, with a heavy-tailed distribution in their "instantaneous" diffusion coefficient δ. The Brownian motion of molecules at thermal equilibrium usually has a finite correlation time and will eventually be randomized after a long delay time τ, so that the central limit theorem applies and the displacement $\Delta x(\tau)$ follows the Gaussian statistics, as was originally envisioned by Saffman and Delbruck (Saffman and Delbrück, 1975). This is true even when the molecules have experienced a complex environment over a finite correlation time. Yet the measured PDF $P(\Delta x)$ for the AChRs is non-Gaussian with an exponential tail, which is independent of the delay time τ, the measured long-time diffusion coefficient D_L (see the discussions of Figure 4a below for the definition of D_L) and the origin and cultured days of the cells.

To explain the observed non-Gaussian statistics and dynamic heterogeneity in living cells, we proposed a dynamic picket-fence (DPF) model (He *et al.*, 2016) of membrane organization involving slow active remodeling of the underlying cortical actin network. As illustrated in Figure 1, we postulated in the DPF model that the immobile and transiently confined transmembrane proteins form a continuous random network, permeating the membrane. Because this (transiently) immobile protein network is anchored to the underlying cortical actin network, the two networks are strongly coupled, with similar structures and dynamics. Recent experiments with electron tomography and super-resolution optical imaging (Novikov *et al.*, 2011; Xu *et al.*, 2012; Fujiwara *et al.*, 2016; Sadegh *et al.*, 2017) revealed that the cortical actin layer underneath the plasma membrane is made of a thin layer of random F-actin network with a variety of meshes (or corrals) of different sizes. Consequently, the (transiently) immobile protein network, which all the mobile membrane molecules, including both transmembrane proteins and lipids, diffuse through, is not uniform and has large spatial variations. In dense regions, where the immobile network has smaller mesh (corral) sizes, the diffusion of mobile membrane molecules is strongly hindered. In light regions, on the other hand, the immobile network has larger mesh (corral) sizes, and hence the mobile membrane molecules diffuse faster. In this way, the immobile protein network produces a unique crowding effect to all membrane molecules, giving rise to a local diffusion coefficient δ, which has a broad (exponential-like) distribution. Because the slow remodeling of the cortical network (and hence the [transiently] immobile protein network) involves active cellular processes (such as myosin motors; Brangwynne *et al.*, 2008; Prost *et al.*, 2015), it is capable of producing fluctuations with a long correlation time, to which the central limit theorem does not apply.

In this paper, we report a comparative study of the lateral motion of ganglioside GM1, which is a glycosphingolipid residing on the outer leaflet of the *Xenopus* muscle cell membrane and thus does not have direct interactions with the underlying cortical actin network. The ganglioside GM1 was recognized as a lipid raft marker in previous single-particle tracking studies (Pinaud *et al.*, 2009). It is found that the GM1s shares the same dynamic heterogeneity and non-Gaussian behavior as the AChRs. This finding supports an important prediction of the DPF model that all the mobile membrane molecules, including lipids and lipid-tethered proteins on the outer leaflet of the cell membrane, should have the same dynamic behavior. Furthermore, we introduce drug treatments to alter the dynamics of the underlying actin network and study their effects on membrane diffusion.

RESULTS

Dynamic heterogeneity of GM1 trajectories

Figure 2a shows a representative collection of 143 GM1 trajectories from a single muscle cell over a duration of 80 s. Two distinct features are observed for the lateral motion of GM1s on the live

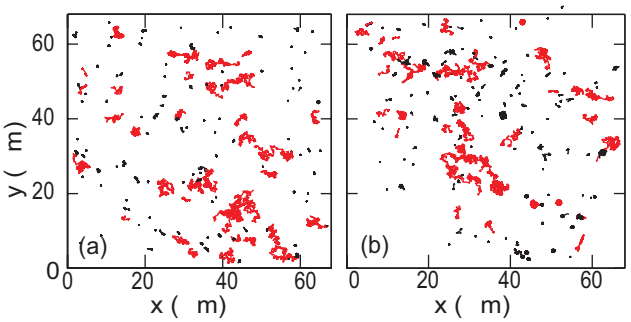

FIGURE 2: (a) One hundred forty-three representative GM1 trajectories with 400 time steps (80 s). (b) One hundred sixty-two AChR trajectories with 400 time steps (80 s). All the trajectories are obtained from the bottom membrane of a *Xenopus* muscle cell with a viewing area 68 × 68 μm^2. Red trajectories indicate fast-moving GM1s/AChRs and black ones indicate nearly immobile GM1s/AChRs.

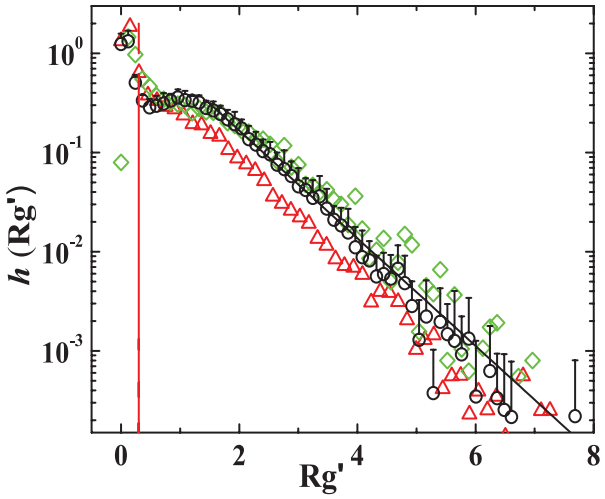

FIGURE 3: Measured PDF (normalized histogram) $h(Rg')$ of the normalized radius of gyration Rg′ for the GM1 trajectories taken at 5 fps (black circles) and 80 fps (green diamonds). The red triangles are obtained from the AChR trajectories taken at 5 fps. Each $h(Rg')$ is obtained by averaging the data from 70 cells under the same condition. The error bars indicate the SD of the measurements. The black solid line shows the exponential function $h(Rg') \simeq 1.5 \exp(-1.25\, Rg')$. The red vertical line indicates the cutoff value $(Rg')c = 0.3$ used to define the immobile trajectories.

cell membrane. First, the size of the GM1 trajectories varies greatly during the same time period, indicating that these identical GM1s exhibit a huge amount of dynamic heterogeneity, some being mobile (red trajectories) and others nearly immobile (black trajectories). Among the mobile GM1s, some move fast (with a large trajectory size) and others slower (with a smaller trajectory size). Second, even the mobile trajectories (red trajectories) contain some transient immobile fragments (thicker red fragments). Similar dynamic heterogeneity was also observed for the AChRs on the same kind of *Xenopus* muscle cells, as shown in Figure 2b.

To have a quantitative description of dynamic heterogeneity of the GM1 trajectories, we calculate their normalized radius of gyration $Rg' = Rg/\langle Rg\rangle$, where $\langle Rg\rangle$ is the mean value of Rg. For Brownian diffusion, one has $\langle Rg\rangle = [(2/3)D_0\tau]^{1/2}$ with D_0 being the diffusion coefficient (He *et al.*, 2016). For the GM1 trajectories, we define $\langle Rg\ (\tau)\rangle = [(2/3)D_L\tau]^{1/2}$, with $D_L = 0.065$ μm^2/s being the long-time diffusion coefficient of the GM1s averaged over 307 muscle cells. By using the normalized Rg', one can compare the GM1 trajectories taken over different τ and/or under different sample conditions.

Figure 3 shows the measured probability density function (PDF or normalized histogram) $h(Rg')$ of Rg' for the GM1 trajectories. The data are obtained by averaging over 70 cells cultured under the same conditions but from different frogs and embryos and on different culture days after dissection. The measured $h(Rg')$s under different sampling rates also collapse onto a single master curve, once the normalized Rg' is used. The measured $h(Rg')$ has a peak at $Rg' \simeq 0.15$ and a plateau region around $Rg' \simeq 1$, followed by a long exponential tail (black solid line), which reveals the large dynamic heterogeneity of the mobile trajectories. The red vertical line indicates the cutoff value $(Rg')c = 0.3$, which is used to define the immobile GM1 trajectories (black trajectories in Figure 2). For comparison, we also show, in Figure 3, the measured $h(Rg')$ for the AChR trajectories (red triangles), which has a shape similar to that for the GM1s.

Anomalous diffusion on live cell membrane

Figure 4a shows the measured MSD $\langle\Delta r^2\ (\tau)\rangle$ as a function of τ for the mobile GM1 trajectories. The data are taken at two sampling rates: 80 fps (red circles) and 5 fps (black circles). To achieve a higher sampling rate, the viewing area of the camera is cropped. Because the immobile GM1s are distributed nonuniformly in space, we find that the measured MSDs at the two sampling rates do not overlap in the common range of τ between 0.2 and 1.25 s. A smooth overlap between the two sets of data is achieved once the immobile trajectories are removed from the ensemble average. In the short-τ region ($\tau < 2$ s), the measured MSD goes as $\langle\Delta r^2\ (\tau)\rangle \sim \tau^\alpha$ with its slope α in the log–log plot varying in the range $0.37 \lesssim \alpha \lesssim 0.91$. Only in the long-τ limit ($\tau > 2$ s) does the measured MSD become diffusive with $\alpha \simeq 1$ (blue solid line). In this case, we have $\langle\Delta r^2\ (\tau)\rangle = 4D_L\tau$, where D_L is the long-time diffusion coefficient of the GM1s. Figure 4a thus reveals a crossover from subdiffusion to normal diffusion.

Also included in Figure 4a are the measured MSDs for the immobile GM1s (green triangles) and stationary QDs (blue diamonds), which are approximately independent of τ. The stationary QDs are physically stuck on a glass coverslip, and thus their MSD provides a noise background, $\langle\Delta r^2\rangle_B \simeq 3.11 \times 10^{-3}$ μm^2 . The measured MSD for the immobile GM1s is $\langle\Delta r^2\rangle_I \simeq 14.7 \times 10^{-3}$ μm^2, which is about half the asymptotic value $\langle\Delta r^2\rangle_0 \simeq 36 \times 10^{-3}$ μm^2 for the mobile GM1s at the $\tau \to 0$ limit. In this limit, the measured MSD becomes the mean square fluctuation, $\left\langle \Delta r_0^2 \right\rangle = \sum_i \left(\left\langle \Delta r^2 \right\rangle_0 \right)$, which is a sum of $(\langle\Delta r^2\rangle_0)_i$ from all independent fluctuation sources *i*. By subtracting the noise background, we find that the immobile GM1s jiggle in a typical range $R_0 = [(\langle\Delta r^2\rangle_I - \langle\Delta r^2\rangle_B)/4]^{1/2} = 60$ nm. A similar value of R_0 was also found for the immobile AChRs (He *et al.*, 2016). We thus conclude that this 50–60 nm–ranged jiggling may result from the agitation of the underlying cortical actin network, to which the immobile GM1s and AChRs are either directly or indirectly bound.

The long-time behavior of $\langle\Delta r^2(\tau)\rangle$ is best presented in the linear plot, as shown in Figure 4b. Because of the optimal imaging condition used and the high efficiency of our tracking algorithm (He *et al.*, 2016), we are able to obtain long-time trajectories of the GM1s with adequate statistics. In a wide range of $2s \lesssim \tau \lesssim 45$ s, in which the GM1s have diffused about 4 μm (or ~4000 times their own diameter), the measured $\langle\Delta r^2(\tau)\rangle$ can be well described by a linear function of τ (red solid line). From the slope of the fitted solid line, we obtain $D_L = 0.092$ μm^2 s^{-1}. For even longer delay times,

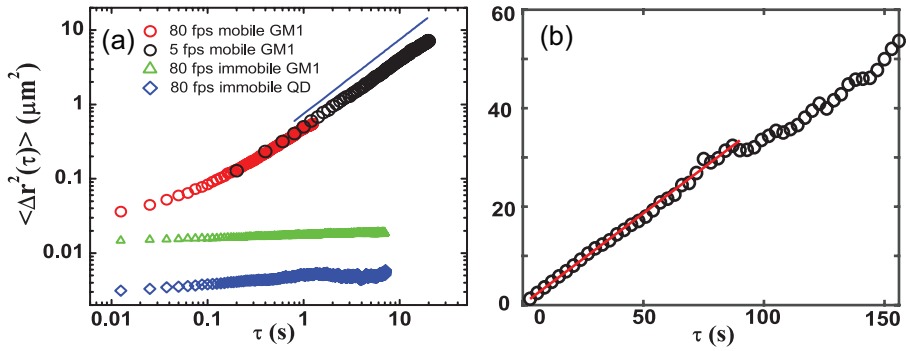

FIGURE 4: (a) Measured MSD $\langle \Delta r^2(\tau) \rangle$ as a function of delay time τ for the mobile GM1 trajectories taken at two sampling rates of 80 fps (red circles) and 5 fps (black circles). The green triangles are obtained from the immobile GM1 trajectories. Data from a single cell are used in the ensemble average. The blue diamonds are obtained from the immobile QDs, which are physically stuck on a coverslip. The blue solid line indicates the relationship $\langle \Delta r^2(\tau) \rangle$ with a slope of unity in the log–log plot. (b) A linear plot of the measured $\langle \Delta r^2(\tau) \rangle$ as a function of τ for the mobile GM1 trajectories taken from a single cell with a sampling rate of 0.25 fps. The red solid line is a linear fit to the data points with $\tau < 45$ s.

$\tau \gtrsim 100$ s, the measured $\langle \Delta r^2(\tau) \rangle$ shows some deviations from the linear fit, which are caused by insufficient statistics in the data set from a single cell.

Membrane proteins in live cells were also found to exhibit subdiffusive behavior (Smith *et al.*, 1999, Kusumi *et al.*, 2005, Ritchie *et al.*, 2005, Weigel *et al.*, 2011), which is often referred to as anomalous diffusion. Because of the limited number and time span of the protein trajectories obtained, however, the measured MSD in some previous studies only revealed a subdiffusive regime without showing a crossover to long-time diffusion. Some of the measurements also suffered relatively large statistical uncertainties at long delay times τ. The MSD shown in Figure 4a clearly reveals crossover behavior from subdiffusion to long-time diffusion with the crossover time $\tau_L \approx 2$ s. In the long-time diffusion regime as shown in Figure 4b, the measured MSD remains as a linear function of τ up to the longest delay time, ~100 s, indicating that the membrane is very fluidic for GM1s (and AChRs). During this time, GM1s diffuse about 6 μm (or ~1000 times their own diameter) and no permanent fence is found at this length scale to confine the motion of GM1s.

Figure 5a shows the distribution of the measured D_L for the GM1s from 307 cells cultured under the same conditions but from different frogs and embryos and on different culture days after dissection. The values of D_L have a fairly narrow distribution with $\langle D_L \rangle_{GM1} = 0.065 \pm 0.034$ $\mu m^2\ s^{-1}$. For comparison, we also include the distribution of the measured D_L for the AChRs from 365 cells. It is seen that the AChRs' distribution has a shape similar to that for the GM1s, but on average the AChRs move more slowly than the GM1s, with $\langle D_L \rangle_{AChR} = 0.041 \pm 0.015$ $\mu m^2\ s^{-1}$.

As shown in Figure 2, both AChRs and GM1s have a considerable number of immobile trajectories, which were assumed to be anchored on the underlying cortical actin network in the DPF model. These immobile molecules, together with other anchored transmembrane proteins, form a (transiently) immobile network at high concentrations, with a structure similar to that of the underlying actin network. As a result, the motion of all mobile (unanchored) membrane molecules, including both transmembrane proteins and lipids, is hindered by this immobile porous network permeating the membrane. The mobile ratio γ, which is defined as the number ratio of the mobile trajectories to the total number of trajectories, reflects the number fraction of the membrane molecules whose dynamics is determined primarily by the confinement of membrane partition. Figure 5b shows the final statistics of the mobile ratio γ of the GM1s from the 307 cells. The distribution of γ is broad, with the mean value $\langle \gamma \rangle_{GM1} = 0.67 \pm 0.16$. The value of γ tends to be smaller for unhealthy cells and for cells cultured over a long period of time. The AChRs have a similar distribution of γ, with the mean value $\langle \gamma \rangle_{AChR} = 0.64 \pm 0.17$ being approximately the same as that for the GM1s.

Non-Gaussian statistics of displacements

We now discuss the statistical properties of the *x*- and *y*-components of the displacement vector $\Delta r(\tau)$ at a fixed value of τ. Figure 6 shows the measured PDFs (normalized histograms), $P(\Delta x')$ and $P(\Delta y')$, as a function of the normalized variables $\Delta x' = \Delta x/(2D_L\tau)^{1/2}$ and $\Delta y' = \Delta y/(2D_L\tau)^{1/2}$, where $(2D_L\tau)^{1/2}$ is the average diffusion length. Although the measured D_L varies considerably under different cell conditions, the measured histograms $P(\Delta x')$ and $P(\Delta y')$ for the mobile GM1s obtained under different sample conditions all collapse onto a single master curve, once the normalized variable $\Delta x'$ (and $\Delta y'$) is used. Except for a sharp peak near the origin, all of the PDFs have an exponential tail, $P(\Delta x') \sim \exp(-\beta|\Delta x'|)$, with $\beta = 1.26$ (red solid line). The error bars show the SD of the black circles averaged over 10 cells. Similar $P(\Delta x')$s (and $P(\Delta y')$s) are also found for the mobile AChRs (He *et al.*, 2016). These experimental results thus demonstrate that GM1s and AChRs have a common exponential PDF $P(\Delta x')$ (and $P(\Delta y')$), which has a universal form among the cells under different sample conditions and is persistent for different values of delay time τ.

It was shown that the exponential PDF $P(\Delta x')$ is directly linked to the fact that the membrane molecules have a broad distribution in their diffusion coefficient. In this case, one can show that (He *et al.*, 2016)

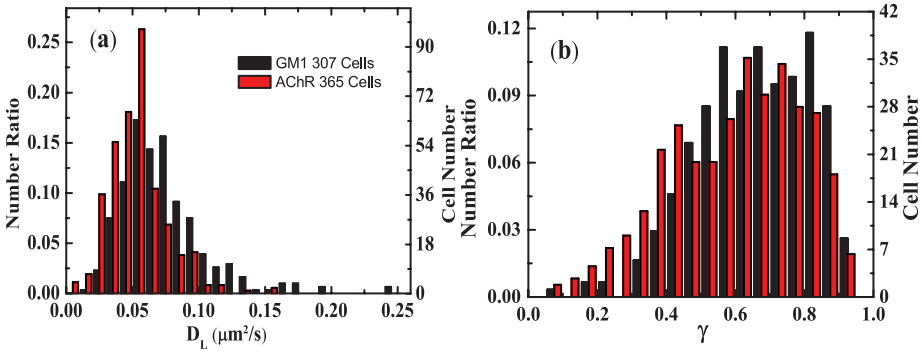

FIGURE 5: (a) Comparison of the distribution of the measured long-time diffusion coefficients D_L of GM1s (black bars) and AChRs (red bars) (b) Comparison of the distribution of measured mobile ratios γ of the GM1s (black bars) and AChRs (red bars).

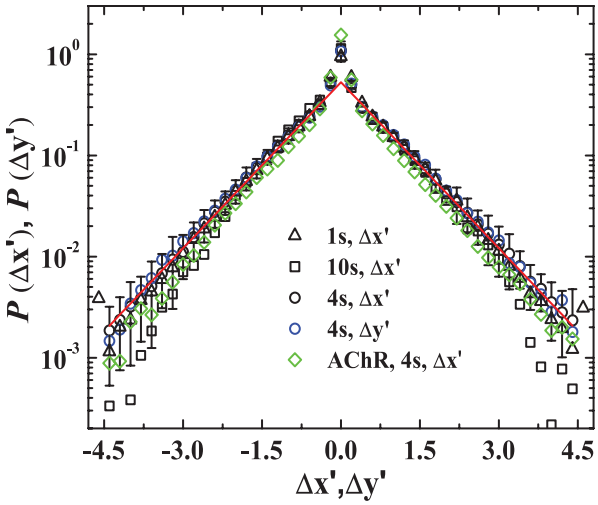

FIGURE 6: Measured PDFs $P(\Delta x')$ and $P(\Delta y')$ of the normalized displacements $\Delta x'$ and $\Delta y'$ for the mobile trajectories of GM1s. The data are obtained from 10 cells under different sample conditions: 1) $\Delta x'(\tau)$ with $\tau = 1$ s (black triangles), 4 s (black circles), and 10 s (black squares); 2) $\Delta y'(\tau)$ with $\tau = 4$ s (blue circles); and 3) $\Delta x'(\tau)$ with $\tau = 4$ s for the mobile trajectories of AChRs from 10 cells (green diamonds). The error bars show the SD of the black circles averaged over 10 cells. The red solid line is an exponential fit to the black circles, $P(\Delta x') \simeq a\exp(-\beta|\Delta x'|)$, with $a = 0.53$ and $\beta = 1.26$.

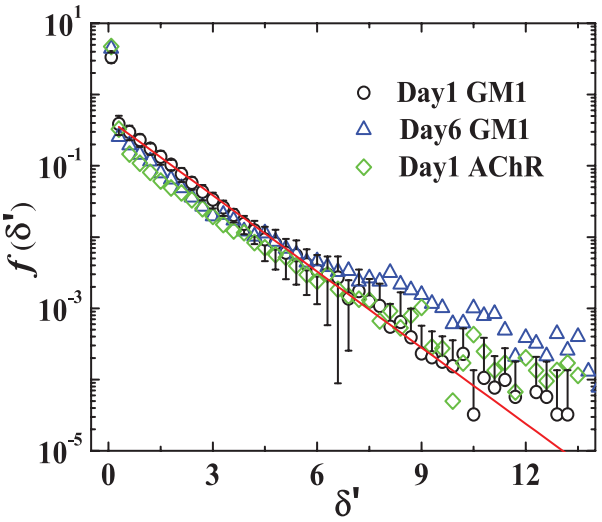

FIGURE 7: Measured PDF $f(\delta')$ of the normalized diffusion coefficient $\delta' = \delta/D_L$ for the mobile GM1 trajectories. The data are obtained from two groups of 10 cells each cultured for 1 day (black circles) and 6 days (blue triangles), respectively. The green diamonds are obtained from the mobile AChR trajectories taken from a group of 10 cells cultured for 1day. The error bars indicate the SD of the black circles averaged over 10 cells. The red solid line is an exponential fit to the black circles, $f(\delta') \simeq 0.45\exp(-0.82\delta')$.

$$P(\Delta x') = \int_0^\infty g(\Delta x;\delta) f_0(\delta)\, d\delta = \frac{1}{\sqrt{2}}\, e^{-\sqrt{2}|\Delta x'|} \quad (1)$$

where each subgroup of membrane molecules is assumed to obey the Gaussian statistics with a diffusion coefficient δ,

$$g(\Delta x;\delta) = \frac{1}{(4\pi\delta\tau)^{1/2}}\, e^{-\Delta x^2/(4\delta\tau)} \quad (2)$$

and δ has an exponential-like distribution,

$$f_0(\delta) = \frac{1}{D_L}\, e^{-\delta/D_L} \quad (3)$$

with D_L being the mean value of δ measured in Figure 4b. The predicted decay rate $\beta = \sqrt{2}$ is very close to the measured $\beta = 1.26$, as shown in Figure 6.

To further test Eq. (1) for the mobile GM1s, we directly measure the "instantaneous" diffusion coefficient $\delta = \langle \Delta r^2(\tau)\rangle t/(4\tau)$ with the delay time $\tau = 1$ s and the averaging time $t = 4.2$ s, above which the measured MSD becomes diffusive (see Figure 4a). Figure 7 shows the measured PDF $f(\delta')$ of the normalized diffusion coefficient $\delta' = \delta/D_L$ for two groups of GM1s under different culture conditions. For comparison, we also include the data for the AChRs from 10 cells. All of the measured PDFs for the cells from different embryos or cultured on different days collapse onto a single master curve, once the normalized δ' is used in the plot. They have a universal shape with a sharp peak for small values of δ' followed by an exponential-like tail (red solid line). The peak near the origin is caused by the immobile fragments in the mobile trajectories. A small deviation of the slope of the measured $f(\delta')$ in the semilog plot from unity is due to sampling fluctuations in the measured δ', which causes broadening of the measured PDFs (Michalet and Berglund, 2012; He *et al.*, 2016). Figure 7 thus confirms that the theoretical prediction given in Equation 2 is a universal mechanism, which applies to both transmembrane proteins (such as AChRs) and lipids on the outer leaflet of the plasma membrane (such as GM1s).

Theoretical models of anomalous diffusion of membrane proteins have considered the effects of diffusion obstruction by permanent or transient obstacles and confinement by transient binding of diffusing proteins to a hierarchy of traps (Kusumi *et al.*, 2005; Saxton, 2007; Höfling and Franosch, 2013; Soula *et al.*, 2013). In the latter case, the time that the protein molecules are confined in the traps was assumed to have a power-law distribution (Wong *et al.*, 2004; Höfling and Franosch, 2013; Meroz and Sokolov, 2015), which gives rise to a nonconverging mean trapping time. For example, Daumas *et al.* (2003) and Destainville *et al.* (2008) discussed how a trapping potential affects the τ-dependence of the measured MSD. Goiko *et al.* (2018) used the continuous-time random walk (CTRW) model to describe the membrane protein motion with a series of random jumps interrupted by "trapping" events with power law–distributed waiting times. While these models can predict certain aspects of anomalous diffusion, such as the subdiffusion exponent α, the present experiment reveals some new features of membrane diffusion, which have not been considered in the previous models. The new features include the persistent exponential tail in the measured PDFs $P(\Delta x')$ (and $P(\Delta y')$), which is invariant with delay time τ, and a crossover to apparently normal diffusion (in terms of MSD) at long delay times ($\tau > 2$ s) but with non-Gaussian statistics.

One could introduce a crossover to normal diffusion by assuming that the trapping time of the protein molecules has an upper bound at equilibrium and thus their correlation time is finite. In this case, the protein trajectories would eventually be randomized at the long-time limit, and their displacement $\Delta x'$ (and $\Delta y'$) would follow the Gaussian statistics. Indeed, such a crossover back to Gaussian statistics has been observed in a variety of dense fluid systems at equilibrium, such as colloidal diffusion near its glass transition (Ghosh *et al.*, 2011; Hunter and Weeks, 2012) and over an external random potential (Hanes *et al.*, 2012). Therefore, a new crossover mechanism is needed to explain the non-Gaussian diffusion dynamics of membrane molecules (including AChRs and GM1s) in the long-time regime. The DPF model assumed that the observed

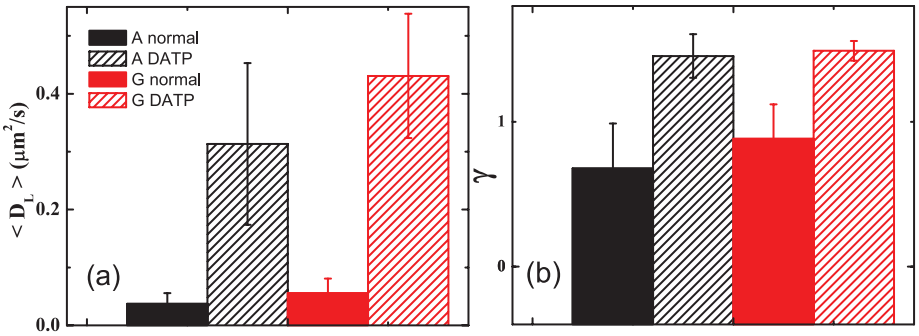

FIGURE 8: (a) Changes of the mean value of the long-time diffusion coefficient D_L for GM1s (black bars) and AChRs (red bars) after ATP depletion (DATP). (b) Changes of the mean value of the mobile ratio γ for GM1s (black bars) and AChRs (red bars) after DATP. The statistics of all the data sets for GM1s in a and b were obtained from 30 ATP-depleted cells in three separate experiments and those for AChRs were obtained from 40 ATP-depleted cells in three separate experiments. The error bars indicate the SD of the measurements. The effect of ATP depletion is shown with the shaded bars in comparison with the data from the untreated (normal) cells shown in solid bars.

non-Gaussian statistics for membrane molecules are linked to the slow active remodeling of the underlying cortical actin network, which involves active cellular processes and thus is capable of producing fluctuations with a long correlation time, to which the central limit theorem does not apply.

Effects of the cortical actin network on membrane diffusion

The above experimental results demonstrate that GM1s and AChRs share the same dynamic heterogeneity and non-Gaussian statistics. This finding provides a strong support for the DPF model, as depicted in Figure 1. The DPF model predicted (He *et al.*, 2016) that the observed dynamic heterogeneity of the membrane molecules is caused by the immobile and transiently confined proteins, which are anchored to the underlying cortical actin network. As a result, all the mobile membrane molecules, including both transmembrane proteins and lipids, will diffuse through this porous network, and the dynamics of membrane diffusion is strongly influenced by the dynamics of the cortical actin network. In the Supplementary Material, we show that our finding that GM1s and AChRs share the same diffusion dynamics is not caused by some other possible effects associated with the imaging conditions and quantum dot labeling used in the experiment.

To further verify the DPF model, we introduce several drug treatments in the experiment to alter the dynamics of the F-actin network. Among the drug treatments, we find that depletion of the adenosine triphosphate (ATP) level in live *Xenopus* muscle cells by 2-deoxy-D-glucose and sodium azide produces the largest effect. Cellular ATP is produced by the phosphorylation of cytosolic substrates in glycolysis and by the Krebs cycle and oxidative phosphorylation in mitochondria. These two sources of ATP production are inhibited by treating the live cells with a 1:1 mixture of 2-deoxy-D-glucose and sodium azide. An important advantage of the ATP depletion treatment is that it has a real-time indicator of the ATP level in living cells, magnesium green (MgGr), so that one can use MgGr to select those cells, which respond most effectively to the drug treatment, for further analysis. The responsive cells used count for about 50% of the cell population. It is important to have such a real-time selection of responsive cells to further reduce errors due to cell-to-cell variations and thus improve the statistical accuracy.

Figure 8 shows a comparison between the measured mean values of $\langle D_L \rangle$ and $\langle \gamma \rangle$ for the GM1s (black bars) from the ATP-depleted cells and those without the ATP depletion treatment. For comparison, we also include the data for the AChRs (red bars) with and without the ATP depletion treatment. It is seen that the depletion of intracellular ATP has a drastic effect on membrane diffusion. The value of the long-time diffusion coefficient D_L for GM1s is increased more than 10 times compared with the control value (0.61 $\mu m^2 s^{-1}$/0.056 $\mu m^2 s^{-1}$ = 10.89). Similarly, the value of $\langle D_L \rangle$ for AChRs is increased more than 13 times (0.51 $\mu m^2 s^{-1}$/0.037 $\mu m^2 s^{-1}$ = 13.78). The value of the mobile ratio $\langle \gamma \rangle$ for GM1s is increased by 45% compared with the control value (0.93/0.64 = 1.45). Similarly, the value of $\langle \gamma \rangle$ for AChRs is increased by 80% (0.97/0.54 = 1.8).

In addition to the large changes in the measured $\langle D_L \rangle$ and $\langle \gamma \rangle$, the ATP depletion also produces a significant change in the statistics of the displacement $\Delta x(\tau)$ (and $\Delta\gamma(\tau)$). Figure 9a shows how the measured PDFs (normalized histograms) $P(\Delta x')$ of the normalized displacement $\Delta x'(\tau)$ for GM1s (black circles) and AChRs (red triangles) change after the ATP depletion. It is seen that the measured $P(\Delta x')$ for both GM1s and AChRs does not have a simple exponential form for normal cells (blue dashed line) any more, and it curves up in the semilog plot with a small increase in $P(\Delta x')$ at small values of $\Delta x'$ and a decrease in $P(\Delta x')$ at large values of $\Delta x'$.

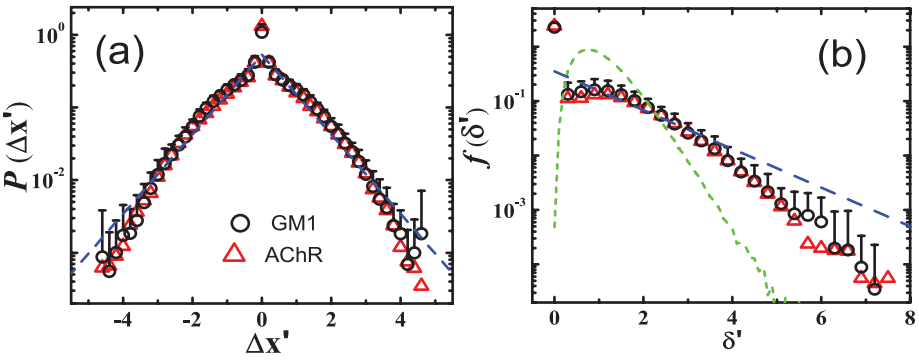

FIGURE 9: (a) Measured PDF $P(\Delta x')$ of the normalized displacement $\Delta x'(\tau)$ with $\tau = 4$ s for the mobile trajectories of GM1s (black circles) and AChRs (red triangles) after ATP depletion (DATP). The blue dashed line indicates the exponential fit, $P(\Delta x') \simeq 0.53 \exp(-1.26|x'|)$, to the black circles shown in Figure 6. (b) Measured PDF $f(\delta')$ of the normalized instantaneous diffusion coefficient $\delta' = \delta/D_L$ for the mobile trajectories of GM1s (black circles) and AChRs (red triangles) after DATP. The blue dashed line indicates the exponential fit, $f(\delta') \simeq 0.45 \exp(-0.82\delta')$, to the black circles shown in Figure 7. The green dashed line shows the measured $f(\delta')$ for the silica spheres undergoing normal Brownian diffusion. The statistics of all the data sets for GM1s in a and b were obtained from 30 ATP-depleted cells in three separate experiments and those for AChRs were obtained from 40 ATP-depleted cells in three separate experiments. All the cells used were cultured within the first two days. The error bars show the SD of the measurement for the black circles.

Such a reduction of dynamic heterogeneity is observed more clearly in the measured histograms $f(\delta')$ of the normalized instantaneous diffusion coefficient $\delta' = \delta/D_L$ for GM1s (black circles) and AChRs (red triangles) after the ATP depletion. The measured $f(\delta')$ for both GM1s and AChRs, as shown in Figure 9b, reveals a significant reduction in its tail part, with high values of $\delta'(\delta' > 3)$ compared with that for normal cells (blue dashed line). After the ATP depletion, the distribution of the measured δ' *becomes* narrower and its shape becomes closer to that of normal Brownian diffusion for dynamically homogenous particles (green dashed line).

These experimental results indicate a general trend that the reduction of the intracellular ATP level seems to weaken the coupling between the plasma membrane and the cortical actin network, reducing the partition of the membrane so that the membrane molecules can diffuse more freely and homogeneously on the cell membrane. As a result, the mobility of the GM1s and AChRs is increased, the immobile fraction of the membrane molecules is decreased, and the level of dynamic heterogeneity and non-Gaussian behavior of the GM1s and AChRs is also significantly reduced. Such a trend of moving toward Gaussian statistics after ATP depletion becomes even more pronounced for the mobile trajectories of the GM1s and AChRs after their immobile segments are removed from the ensemble average (Su, 2017).

To examine what actually happened to the cortical actin network, we use a fluorescently tagged phalloidin (Rhodamine-phalloidin) to visualize the F-actin network inside the muscle cells. Figure 10 shows how the F-actin network inside the muscle cells changes after the treatment of ATP depletion. In the untreated (normal) muscle cell, actin filaments are abundant (see Figure 10a) and they form sarcomeres, which are observed in Figure 10b as fine periodic bands along the thick fibrils (Brennan *et al.*, 2005). In addition, F-actin filaments are abundant underneath the cell membrane in the peripheral region, and they support filopodial and lamellipodial protrusions. In the ATP depleted muscle cell, actin filaments remain abundant in the bulk region of the cell (see Figure 10c). But there is a depletion region developed between the cell boundary and the bulk region, in which the fluorescence intensity of the cortical F-actin network is diminished (see Figure 10d).

To quantify the intensity changes of the stained F-actin network in the cortical region, we compute the ratio R of the measured fluorescent intensity in the bulk region to that in the cortical region. The blue and red boxes in Figure 10, b and d, show, respectively, a sampled cortical region and an adjacent bulk region further away from the cell boundary. The value of R is sampled over different parts of 20 muscle cells for both the ATP depleted and control cell sets. Sixty pairs of boxes are used in the statistics under each condition. Figure 11 shows how the intensity ratio R changes after ATP depletion. It is seen that for the untreated (normal) cells, the measured fluorescent intensity of the stained F-actin network in the cortical region is approximately the same as that in the bulk region, with $R = 0.96 \pm 0.18$. For the ATP depleted cells, however, we find $R = 2.62 \pm 0.79$, indicating that the content of F-actin in the cortical region is severely depleted by the reduction of the cellular ATP level. The loss of cortical actin after the ATP depletion was also reported for other cell types (Mandel *et al.*, 1994; Prahalad *et al.*, 2004).

The actin cortex is a densely packed thin layer of actin filaments and actin-binding proteins approximately 1 μm in thickness (Xu *et al.*, 2012; Clark *et al.*, 2013). The actin filaments and myosin II motor proteins in this region work together to generate forces for cell shape change, cytokinesis, and cell migration (Bray and White, 1988) via two active cellular processes driven by ATP hydrolysis: the actin filament polymerization/depolymerization (also called tread milling) and myosin motor contraction (Bugyi and Carlier, 2010). We believe that the main effects of the ATP depletion, as shown in Figures 9–11, are most likely caused by the disruption of cortical F-actin assembly (e.g., reduction of actin polymerization), which gives

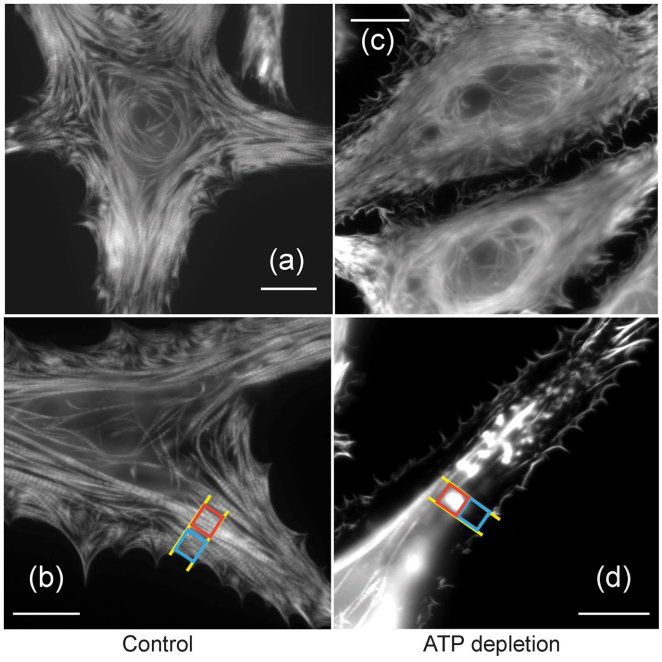

FIGURE 10: Microscope images of the rhodamine–phalloidin stained F-actin filaments in a cultured *Xenopus* muscle cell. (a) Large view of an untreated (normal) cell; (b) enlarged view of a portion of the normal muscle cell; (c) large view of an entire cell (top portion of the image) after the ATP depletion; (d) enlarged view of a portion of the muscle cell after the ATP depletion, showing the local feature of F-actin filaments. All of the scale bars are 20 μm. The blue and red boxes in b and d show, respectively, a sampled cortical region and an adjacent bulk region further away from the cell boundary. Each box covers an area of 5×5 μm^2, and they are aligned along the normal direction of the cell boundary, as indicated by the two parallel yellow lines.

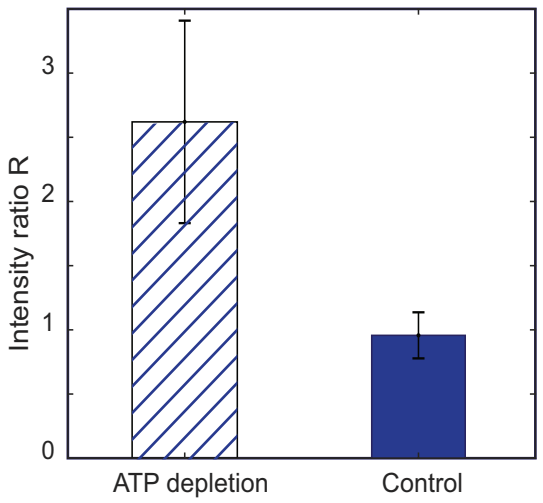

FIGURE 11: Changes in the measured fluorescent intensity ratio R after the ATP depletion. The value of R is averaged over different parts of 20 muscle cells for both the ATP-depleted and control cell sets. Sixty data points are used in the statistics under each condition. The error bars show the SD of the measurements.

rise to a much weakened actin network in the cortical region of the cell. This conclusion can also explain the observed suppression of nonthermal motion of the cortical network by ATP depletion, as reported in recent rheology measurements (Hoffman *et al.*, 2006; Van Citters *et al.*, 2006).

The weakening of the cortical actin network reduces the anchoring probability of membrane proteins to the underlying actin cortex. As a result, almost all the AChRs and GM1s become mobile, with $\langle\gamma\rangle > 0.93$, and their values of $\langle D_L\rangle$ increase by a factor of more than 10. Large changes in the diffusion coefficient were also observed in other experiments when the coupling between the plasma membrane and the underlying cortical actin network was altered significantly. For example, Fujiwara *et al.* (2016) reported that the diffusion coefficient of the transferrin receptors (TfRs) and phospholipid molecules (DOPEs) on the blebbed membrane (detached from the cortical actin network) is increased by more than 25 times from that for normal NRK cells. These results provide further support for our conclusion that the changes in the measured $\langle D_L\rangle$ and $\langle\gamma\rangle$ for GM1s and AChRs after, ATP depletion are linked to the decoupling of the cortical actin network with the plasma membrane. In a recent review article, Kusumi *et al.* (2012) showed that the diffusion coefficient of lipid molecules in artificial membranes (freestanding membranes without an immobile protein network) is comparable to that in blebbed membranes. While the blebbed membranes and artificial membranes have different compositions and membrane structures, the fact that their diffusion coefficients are comparable and are more than 20 times larger than that in plasma membranes supports our observation that the immobile protein network, which is absent in both blebbed membranes and artificial membranes, plays a dominant role in determining the diffusion coefficient in plasma membranes.

Figures 10 and 11 thus provide structural evidence showing that the ATP depletion significantly reduces the direct coupling between the plasma membrane and actin network in the cortical region of the cell. While details about the structural attachment and interactions between the actin cortex and plasma membrane still need to be clarified (Charras *et al.*, 2006), our experiment clearly reveals that the membrane partition and diffusion in living cells are regulated via the active control of actin dynamics in the cortical region, which requires a constant flux of energy resulting from ATP hydrolysis.

Besides the ATP depletion, we also performed other drug treatments to alter the dynamics of the F-actin network (He, 2015). Treatment with latrunculin A is known to reduce polymerization of F-actin and disrupt the actin network (Coué *et al.*, 1987). As a result, the probability of membrane proteins anchoring to the underlying actin cortex is reduced. We find that treatment with 3 µM latrunculin A for 2 h resulted in an increase of the mobile ratio γ by 60% and 16%, respectively, for AChRs and GM1s relative to the control values. The value of D_L is increased by 31% for AChRs and by 22% for GM1s. Treatment of jasplakinolide in vivo also involves reduction of F-actin (Bubb *et al.*, 2000). Under treatment with 50 nM jasplakinolide for 2 h, the mobile ratio γ is found to increase by 41% and 6%, respectively, for AChRs and GM1s relative to the control values. The value of D_L is increased by 72% for AChRs and by 56% for GM1s.

Treatment of widespread cells such as cultured muscle cells with nonmuscle myosin II inhibitors, such as blebbistatin and Y27632, was found to enhance the cortical actin network and increase its thickness (Cai *et al.*, 2010; Kumar *et al.*, 2019). We find that treatment with 100 µM blebbistatin for 2 h resulted in a decrease of the mobile ratio γ by 4% and 66%, respectively, for AChRs and GM1s relative to the control values. The value of D_L was decreased by 17% for AChRs and by 73% for GM1s. Under treatment with 180 µM Y27632 for 1–2 h, the mobile ratio γ was found to decrease by 39% and 60%, respectively, for AChRs and GM1s relative to the control values. The value of D_L was decreased by 12% for AChRs and by 63% for GM1s.

Treatment with tyrosine phosphatase inhibitor pervanadate is known to increase phosphorylation in the rapsyn-MuSK pathway (Mohamed *et al.*, 2001). From the phalloidin-stained images, we find that under treatment with 40 µM pervanadate for 1 h, the cortical actin network collapsed partially, with formation of a number of large actin clusters, together with a large decrease in actin density in most other areas. Treatment with 10 mM pervanadate resulted in complete disruption of the F-actin network. Our AChR tracking measurements reveal that under treatment with 40 µM pervanadate for 1 h, the mobile ratio γ increased by 56% from the control value. The value of D_L increased by 51% for AChRs.

While these drug treatments made various degrees of change in the diffusion dynamics of GM1s and AChRs, they reveal a general trend that when the coupling between the plasma membrane and the cortical actin network is weakened by drug treatments, the probability of membrane proteins anchoring to the underlying actin cortex is reduced, so that the immobile membrane protein network is weakened. Consequently, both the mobile ratio γ and the diffusion coefficient D_L are increased from the control values. On the other hand, when the coupling between the plasma membrane and the cortical actin network is enhanced by drug treatments, the probability of membrane proteins anchoring to the underlying actin cortex is increased, and consequently, both the mobile ratio γ and the diffusion coefficient D_L are reduced because of the enhanced immobile membrane protein network.

DISCUSSION

In the above, we described a comparative study of the lateral motion of lipid molecules and transmembrane proteins, both residing on the plasma membranes of live *Xenopus* muscle cells. The lipid chosen for the study was the ganglioside GM1, which is a glycosphingolipid residing on the outer leaflet of the plasma membrane and thus does not have direct interactions with the underlying cortical actin network. The protein used for the study was acetylcholine receptor (AChR), which is a well-characterized ion channel having direct interactions with the cortical actin network. By accurately tracking a large volume of individual molecular trajectories from more than 300 live cells over a wide range of sampling rates (up to 80 fps) and long delay times (up to 200 s), we were able to obtain a number of high-order statistical measures of the molecular displacement $\Delta x(\tau)$ over a long delay time τ, such as the mean squared displacement (MSD) $\langle \Delta r^2(\tau)\rangle$, probability density function (PDF or normalized histogram) $P(\Delta x)$, PDF $h(R_g)$ of the radius of gyration R_g, and PDF $f(\delta)$ of the local diffusion coefficient δ. From these statistical analyses, we demonstrate that the GM1s and AChRs share the same dynamic heterogeneity and non-Gaussian statistics. They are also found to have similar distributions of the mobile ratio γ (~65%) and long-time diffusion coefficient D_L for cells cultured under the same conditions.

The local diffusion of a membrane molecule is determined primarily by the crowding effect imposed by its surrounding molecules (Destainville *et al.*, 2008; Kusumi *et al.*, 2012; Höfling and Franosch, 2013; Jacobson *et al.*, 2019). Because of the complexity of the membrane structures, however, a membrane molecule will interact with many different molecules in its surroundings, both "horizontally" with other membrane proteins/lipids and "vertically" with the actin cortex and pericellular matrix (which is not studied in the present work). As a result, macromolecular crowding, which is a common term used in the biophysics community, may have different

meanings. A main finding of our experiments is that among different crowding effects, the immobile and transiently confined proteins play a dominant role in determining the membrane diffusion. The diffusion coefficient of mobile AChRs and GM1s is increased by more than a factor of 10 when the immobile ratio of membrane molecules (including AChRs and GM1s) is reduced by ATP depletion. Previous studies also reported that the diffusion coefficient of membrane proteins/lipids on the blebbed membrane (detached from the actin cortex) is increased by more than 25 times from that for normal cells (Fujiwara *et al.*, 2016). Furthermore, our measurements reveal that the diffusion coefficients of mobile AChRs and GM1s are similar, indicating that the direct interactions between the mobile (unanchored) AChRs and actin cortex do not play a significant role in determining the diffusion coefficients of transmembrane proteins.

Based on these results, we conclude that 1) the concentration of immobile and transiently confined proteins on the membrane must be large in order to produce such a large change in membrane diffusivity; 2) because these immobile proteins are anchored to the underlying cortical actin network, they will form a (transiently) immobile network at high concentrations (Fujiwara *et al.*, 2016) with a structure similar to that of the underlying actin network. As the immobile protein network is embedded in the membrane, all the mobile membrane molecules will diffuse through this largely 2D porous network. In this way, the immobile protein network produces a unique crowding effect on all membrane molecules, including both transmembrane proteins and lipids. Figure 7 reveals that the local diffusion coefficient has a broad (exponential-like) distribution with its value varying by a factor of more than 10, suggesting that the immobile protein network is not uniform and has large spatial variations. In concentrated regions, where the immobile network has smaller mesh (corral) sizes, the diffusion of mobile membrane molecules is strongly hindered. In dilute regions, on the other hand, the immobile network has larger mesh (corral) sizes, and hence the mobile membrane molecules diffuse faster. As mentioned above, the large difference in diffusivity between the normal cell membrane and the blebbed membrane provides a wide dynamic range for variations of the local diffusion coefficient δ.

These findings provide strong support for the dynamic picket-fence (DPF) model, as depicted in Figure 1. The DPF model (He *et al.*, 2016) was originated from the picket-fence model (Kusumi *et al.*, 2005; Ritchie *et al.*, 2005), which envisioned that the cortical actin "fences" and anchoring protein "pickets" are permanent structures on the membrane and the mobile proteins can only hop between different corrals of the cortical actin fences following a thermal activation process (Fujiwara *et al.*, 2002). Although this hop diffusion model can qualitatively explain some previous single molecule–tracking results, it contains several key assumptions that are inconsistent with the findings of the recent (He *et al.*, 2016) and present experiments. First, the model assumed that the corrals are quasi-periodic, with a narrow size range between 32 and 230 nm, depending on the cell type (Kusumi *et al.*, 2005; Ritchie *et al.*, 2005; Kraft, 2013). It is difficult to produce a broad exponential-like distribution $f(\delta)$, as shown in Figure 7, when the immobile protein network is spatially homogeneous with a narrow distribution of mesh sizes. Second, our measurements reveal that the diffusion coefficients of mobile AChRs and GM1s are similar, indicating that the direct interactions between the mobile (unanchored) AChRs and actin cortex do not play a significant role in determining the diffusion coefficient of transmembrane proteins. As mentioned above, a main finding of our experiments is that among different crowding effects, the immobile proteins (both permanently and transiently confined) play a dominant role in determining membrane diffusion. As a result, activated hopping over the cortical actin fences is unlikely to play a major role in slowing down the diffusion of mobile membrane molecules. Finally, the picket-fence model assumed that the hopping of membrane molecules between different corrals is caused by thermal fluctuations, an equilibrium process with a finite correlation time that is unlikely to produce non-Gaussian statistics at the long-time limit, as shown in Figure 6.

To overcome these shortcomings, the DPF model hypothesizes that the anchored protein network permeating the membrane is neither spatially homogeneous nor temporally frozen. It is only transiently immobile and its long-time dynamics is determined by the underlying cortical actin network, which is under slow active remodeling (Gowrishankar *et al.*, 2012; Luo *et al.*, 2013; Guo *et al.*, 2014; Parry *et al.*, 2014). Consequently, membrane diffusion is expected to be strongly influenced by the dynamics of the cortical actin network, which requires a continuing energy input. Our measurements with the ATP-depleted cells reveal that the diffusion dynamics of the GM1s and AChRs is indeed evenly affected by the intracellular ATP level of the living muscle cells. It is found that ATP depletion significantly reduces direct coupling between the plasma membrane and the cortical actin layer, leading to a significant reduction of membrane partitioning. As a result, the mobile ratios of both the GM1s and AChRs and their mobility on the membrane are all significantly increased, and the levels of dynamic heterogeneity and non-Gaussian behavior of the GM1s and AChRs are reduced.

Our conclusion on membrane diffusion through a heterogeneous and slow-varying protein network is also supported by recent studies of the structure and dynamics of the cortical actin network. It was shown by recent electron tomography and superresolution optical imaging (Xu *et al.*, 2012; Fujiwara *et al.*, 2016; Sadegh *et al.*, 2017) that the cortical actin layer underneath the plasma membrane is a thin layer of random F-actin network with a large variety of meshes (corrals) of different sizes. Mobile proteins in the membrane diffuse through the corrals (Andrews *et al.*, 2008; Sadegh *et al.*, 2017). In a more recent experiment, Freeman *et al.* (2018) used an actin picket–tethering protein to manipulate the direct coupling between a transmembrane protein and the cortical actin network. It was found that when the actin-picket-tethering proteins were removed from the cortical region, membrane partition/hindering was reduced and both the membrane proteins and the lipids in the outer leaflet of the membrane diffuse more freely. This observation is consistent with our finding on the ATP depletion effect. From simultaneous observations of the motion of the QD-labeled IgE receptors and GFP-tagged actin dynamics in the cortical region, Andrews *et al.* (2008) reported that the active remodeling of large-scale actin structures in the cortical region occurs over seconds, making the location and dimension of actin-defined corrals time-dependent. It was also shown (Andrews *et al.*, 2008) that disruption of the actin cytoskeleton by latrunculin B resulted in an increased diffusion of the receptor clusters. These results further support our finding that the cortical actin network not only provides a fence for membrane compartmentalization that restricts diffusion of all membrane molecules (such as AChRs and GM1s), but also dynamically influences their long-term mobility and nonequilibrium statistics.

Our experiment thus provides an interesting example showing how membrane diffusion is actively regulated in living cells via the actin dynamics in the cortical region, which requires a constant input of energy from ATP hydrolysis. Although the DPF model is primarily qualitative, it provides a framework of key factors that can qualitatively explain the main features observed in the experiment. It also lays a foundation for further development of theoretical models to

describe the diffusion dynamics of mobile membrane molecules quantitatively through a heterogeneous protein network that is anchored to the underlying cortical actin network under slow active remodeling.

MATERIALS AND METHODS

Primary cell culture

Ganglioside GM1s are abundant on the plasma membranes of *Xenopus* muscle cells, which were dissected from myotomes of the fertilized *Xenopus* embryos developed at stages 20–22, following the protocol described in Peng *et al.* (1991). The dissected muscle cells were seeded on circular glass cover slips coated with entactin, collagen IV, and laminin (ECL, purchased from Upstate Co.) and were cultured in a medium consisting of 88% Steinberg's solution, 10% L-15 medium (purchased from Leibovitz Co.), 1% fetal bovine serum, and 1% penicillin/streptomycin/gentamicin (Sigma Aldrich). The primary cultured muscle cells were spread on the ECL coating after 24 h. The muscle cell cultures were maintained at 23°C and could be stored for 3 wk if they were not contaminated.

Quantum dot labeling

To track the GM1s on the membrane of a living muscle cell, the individual GM1s were labeled with bright and photostable fluorescent quantum dots (QDs; Bannai *et al.*, 2006; Geng, 2006). This was achieved by first labeling the GM1s with biotin-conjugated cholera toxin B subunits (biotin-CTX, C34779, purchased from Invitrogen Co.) for 10 min. GM1 is a specific receptor for cholera toxin. The cells were then washed three times with the culture medium (5 min each) to remove the unbound biotin-CTX. The concentration of biotin-CTX applied to the cells was adjusted according to the final labeling density of the QDs needed. Typically, 0.5 nM biotin-CTX was used for a fast movie recording (80 and 5 fps), and 0.25 nM biotin-CTX was used for a slow movie recording (0.33 fps). A lower concentration of QDs was used to reduce tracking ambiguities between the consecutive images of the QDs. After the repeated washes, the cultures labeled with biotin-CTX were treated for 10 min with 2.5 nM streptavidin-conjugated QD solution (QD655, Q10121MP, purchased from Invitrogen Co.). The cells were then washed three times with the culture medium (5 min each) to remove the unbounded QDs. The entire staining process takes about 1.5 h.

Sample preparation and microscope imaging

The circular coverslip with the QD-labeled living cells was glued onto a stainless steel slide 2 mm thick for microscope imaging. The slide had a central hole of volume 50 µl, which served as a chamber to hold the culture medium and to make optical observations. The living cells were kept in a healthy state for at least 2 h. The live-cell sample was placed on the stage of an inverted microscope (Leica DM-IRB), and the motion of QDs (and hence GM1s) was viewed from below with fluorescence microscopy. Image sequences were recorded using an electron-multiplying charge-coupled device (EMCCD) camera (Andor Ixon3 897 back-illuminated EMCCD) and streamed to the hard drive of a host computer.

Image acquisition was controlled by IQ 3.1 software (Andor Technology). The QDs were excited by visible light with wavelength 400–450 nm, and the light emitted by the QDs was selected to be in the wavelength range 645–655 nm. Typical frame rates used in the movie recording were 5 and 80 fps, and the corresponding exposure times were 30 and 10 ms, respectively. The recorded images have a spatial resolution of 512 × 512 pixels at frame rate 5 fps and 500 × 200 pixels at 80 fps. With a 100 × oil objective (NA = 1.4), the QDs in the image taken at 80 fps typically occupy 5 pixels across their diameter.

As mentioned above, the QD-labeled GM1s were abundant on the membranes of the quiescent muscle cells. In particular, the bottom sides of the membranes facing the substrate were flat and had a large area (up to 0.05 mm^2) for optical observation. This was an optimal situation for tracking a large number of GM1s concurrently. This is true even for samples that were sparsely labeled to avoid trajectory entanglement. For a typical GM1 tracking on the bottom membrane at 5 fps, about 200 QDs were tracked simultaneously for 1000 frames, which typically yielded 1000–3000 (broken) QD trajectories. A total of 2000 images were taken for the 80 fps recording. Long-time GM1 tracking was done at 0.25 fps for 450 frames with a total 30-min recording. For the movie files with the recording time extended to 30 min, the exposure time was carefully controlled to reduce damage to the live-cell samples. Typically, the QD trajectories taken from at least 10 cells cultured under the same conditions were used for statistical analyses. In some cases, such as that shown in Figure 5, we used all the data sets taken from 307 cells.

Single-molecule tracking

A homemade Matlab program based on the standard tracking algorithm (Crocker and Grier, 1996; Anthony *et al.*, 2006; He *et al.*, 2016) was used to determine the GM1 position $r(t)$ at time t, and the GM1 trajectories were constructed from the consecutive images. From the movie of stationary QDs (stuck on a glass slide), we find that their displacement over a time period of 200 s is less than 24 nm (≈ 0.18 pixel). This result sets the accuracy of the measurement of the two-dimensional (2D) displacement vector, $\Delta r(\tau) = r(t + \tau) - (t)$, where τ ($\lesssim$180 s) is the delay time used in the experiment. During this delay time, GM1s moved several micrometers. Because the viscosity of the plasma membrane was ~500 times higher than that of the extracellular medium, the motion of the QD-labeled GM1s was determined primarily by their transmembrane domains (see the Supplementary Material for more discussions).

From the GM1 trajectories, we compute the statistics of $\Delta r(\tau)$, such as the mean squared displacement (MSD) $\langle \Delta r^2(\tau) \rangle$ and the probability density function (PDF) $P(\Delta x)$ of the x-component of $(\Delta r(\tau)$. We also compute the radius of gyration R_g of the GM1 trajectories,

$$R_g^2 = \frac{1}{N}\sum_i^N \left[(x_i - x)^2 + (y_i - y)^2 \right] \quad (4)$$

where N is the total number of time steps in each trajectory, x_i and y_i are the projections of the position of each trajectory step on the x- and y-axis, respectively, and x and y are their mean values. Physically, R_g quantifies the size of a GM1 trajectory generated during the time lapse τ. Other details about the image processing and single-molecule tracking have been described in He *et al.* (2016).

ATP depletion and F-actin staining

We used 2-deoxy-D-glucose (Sigma) and sodium azide (NaN_3, Sigma) to reduce the adenosine triphosphate (ATP) level of the living *Xenopus* muscle cells. It is known that 2-deoxy-D-glucose effectively interrupts anaerobic glycolysis (Jung Hwan *et al.*, 2015) and the metabolic inhibitor NaN_3 (Gribble *et al.*, 1997; Garg and Sanguinetti, 2014) inhibits oxidative phosphorylation by cytochrome oxidase in the mitochondria. Because of inhibition of the two major ATP synthesis sources by the two drugs, the muscle cells will suffer a large decrease in intracellular ATP. The live cells are treated with a 1:1 mixture of the two drugs at 30 mM and incubated for 2 h to allow their ATP stock to be consumed. A similar protocol of ATP depletion has been used in previous experiments (Hoffman *et al.*, 2006; Van Citters *et al.*, 2006).

To monitor the intracellular ATP level of the living muscle cells, the cells were incubated with 10 μM magnesium green-AMester (MgGr, Molecular Probes) for 30 min in the dark and washed three times with culture medium (1 min each). The MgGr has an absorption (emission) maximum at approximately 506 nm (531 nm). Because ATP has a higher affinity for Mg^{2+} than ADP (Leyssens *et al.*, 1996; Bernstein and Bamburg, 2003; Lee and Peng, 2007) and the emission intensity of MgGr increases when it binds to free intracellular Mg^{2+}, the fluorescence intensity of MgGr is inversely correlated to the intracellular ATP level. As a result, we selected those cells with the brightest fluorescence signal as the ones most responsive to the ATP depletion treatment.

To visualize the F-actin network, the muscle cells were fixed with 4% paraformaldehyde in PBS for 15 min at room temperature and washed with PBS three times (1 min each). The muscle cells were then permeabilized with Triton X-100 at a concentration of 0.2% for 5 min and washed three times with PBS (1 min each). The cells were further treated with rhodamine phalloidin for 40 min in the dark and washed three times with PBS (1 min each). After extra water on the cover slips was removed, they were sealed on a glass microscope slide with clear nail polish. The glass slides were pretreated with a drop (3 μl) of anti-photobleaching citifluor solution before the sealing.

ACKNOWLEDGMENTS

The authors wish to thank Yusheng Shen for useful discussions. This work was supported by the Hong Kong RGC under Grants 16302816, 16306418 and 16302718.

REFERENCES

Alcor D, Gouzer G, Triller A (2009). Single-particle tracking methods for the study of membrane receptors dynamics. Eur J Neurosci 30, 987–997.

Almarza G, Sánchez F, Barrantes FJ (2014). Transient cholesterol effects on nicotinic acetylcholine receptor cell-surface mobility. PLoS One 9, e100346.

Andrews NL, Lidke KA, Pfeiffer JR, Burns AR, Wilson BS, Oliver JM, Lidke DS (2008). Actin restricts FcεRI diffusion and facilitates antigen-induced receptor immobilization. Nat Cell Biol 10, 955–963.

Anthony S, Zhang L, Granick S (2006). Methods to track single-molecule trajectories. Langmuir 22, 5266–5272.

Bannai H, Lévi S, Schweizer C, Dahan M, Triller A (2006). Imaging the lateral diffusion of membrane molecules with quantum dots. Nat Protoc 1, 2628–2634.

Barrantes FJ (2014). Cell-surface translational dynamics of nicotinic acetylcholine receptors. Front Synaptic Neurosci 6.

Bernstein BW, Bamburg JR (2003). Actin–ATP hydrolysis is a major energy drain for neurons. J Neurosci 23, 1.

Bloch RJ, Geiger B (1980). The localization of acetylcholine receptor clusters in areas of cell–substrate contact in cultures of rat myotubes. Cell 21, 25–35.

Brangwynne CP, Koenderink GH, Mackintosh FC, Weitz DA (2008). Cytoplasmic diffusion: molecular motors mix it up. J Cell Biol 183, 583.

Bray D, White JG (1988). Cortical flow in animal cells. Science 239, 883.

Brennan C, Mangoli M, Dyer CEF, Ashworth R (2005). Acetylcholine and calcium signalling regulates muscle fibre formation in the zebrafish embryo. J Cell Sci 118, 5181.

Bubb MR, Spector I, Beyer BB, Fosen KM (2000). Effects of jasplakinolide on the kinetics of actin polymerization: an explanation for certain in vivo observations. J Biol Chem 275, 5163–5170.

Bugyi B, Carlier M-F (2010). Control of actin filament treadmilling in cell motility. Annu Rev Biophys 39, 449–470.

Cai Y, Rossier O, Gauthier NC, Biais N, Fardin M-A, Zhang X, Miller LW, Ladoux B, Cornish VW, Sheetz MP (2010). Cytoskeletal coherence requires myosin-IIA contractility. J Cell Sci 123, 413.

Charras GT, Hu C-K, Coughlin M, Mitchison TJ (2006). Reassembly of contractile actin cortex in cell blebs. J Cell Biol 175, 477.

Clark AG, Dierkes K, Paluch EWAK (2013). Monitoring actin cortex thickness in live cells. Biophys J 105, 570–580.

Coué M, Brenner SL, Spector I, Korn ED (1987). Inhibition of actin polymerization by latrunculin A. FEBS Lett, 213, 316–318.

Crocker JC, Grier DG (1996). Methods of digital video microscopy for colloidal studies. J Colloid Interface Sci 179, 298–310.

Daumas F, Destainville N, Millot C, Lopez A, Dean D, Salomé L (2003). Confined diffusion without fences of a G-protein-coupled receptor as revealed by single particle tracking. Biophys J 84, 356–366.

Destainville N, Dumas F, Salomé L (2008). What do diffusion measurements tell us about membrane compartmentalisation? emergence of the role of interprotein interactions. J Chem Biol 1, 37–48.

Engelman DM (2005). Membranes are more mosaic than fluid. Nature 438, 578–580.

Freeman SA, Vega A, Riedl M, Collins RF, Ostrowski PP, Woods EC, Bertozzi CR, Tammi MI, Lidke DS, Johnson P, *et al.* (2018). Transmembrane pickets connect cyto- and pericellular skeletons forming barriers to receptor engagement. Cell 172, 305–317.e10.

Fujiwara T, Ritchie K, Murakoshi H, Jacobson K, Kusumi A (2002). Phospholipids undergo hop diffusion in compartmentalized cell membrane. J Cell Biol 157, 1071.

Fujiwara TK, Iwasawa K, Kalay Z, Tsunoyama TA, Watanabe Y, Umemura YM, Murakoshi H, Suzuki KGN, Nemoto YL, Morone N, Kusumi A (2016). Confined diffusion of transmembrane proteins and lipids induced by the same actin meshwork lining the plasma membrane. Mol Biol Cell 27, 1101–1119.

Garg P, Sanguinetti MC (2014). Intracellular ATP does not inhibit Slo2.1 K+ channels. Physiol Rep 2, e12118.

Gelles J, Schnapp BJ, Sheetz MP (1988). Tracking kinesin-driven movements with nanometre-scale precision. Nature 331, 450–453.

Geng L (2006). Visualization of Nicotinic Acetylcholine Receptor Trafficking with Quantum Dots in Xenopus Muscle Cells. PhD Thesis, Hong Kong University of Science and Technology.

Geng L, Zhang HL, Peng HB (2009). The formation of acetylcholine receptor clusters visualized with quantum dots. BMC Neurosci 10, 80.

Gerrow K, Triller A (2010). Synaptic stability and plasticity in a floating world. Curr Opin Neurobiol, 20, 631–639.

Ghosh A, Chikkadi V, Schall P, Bonn D (2011). Connecting structural relaxation with the low frequency modes in a hard-sphere colloidal glass. Phys Rev Lett 107, 188303.

Goiko M, De Bruyn JR, Heit B (2018). Membrane diffusion occurs by continuous-time random walk sustained by vesicular trafficking. Biophys J 114, 2887–2899.

Gowrishankar K, Ghosh S, Saha SC,R, Mayor S, Rao M (2012). Active remodeling of cortical actin regulates spatiotemporal organization of cell surface molecules. Cell 149, 1353–1367.

Gribble FM, Ashfield R, Ammälä C, Ashcroft FM (1997). Properties of cloned ATP-sensitive K+ currents expressed in *Xenopus* oocytes. J Physiol 498, 87–98.

Groc L, Heine M, Cognet L, Brickley K, Stephenson FA, Lounis B, Choquet D (2004). Differential activity-dependent regulation of the lateral mobilities of AMPA and NMDA receptors. Nat Neurosci 7, 695–696.

Groc L, Lafourcade M, Heine M, Renner M, Racine V, Sibarita J-B, Lounis B, Choquet D, Cognet L (2007). Surface trafficking of neurotransmitter receptor: comparison between single-molecule/quantum dot strategies. J Neurosci 27, 12433.

Guo M, Ehrlicher AJ, Jensen MH, Renz M, Moore JR, Goldman RD, Lippincott-Schwartz J, Mackintosh FC, Weitz DA (2014). Probing the stochastic, motor-driven properties of the cytoplasm using force spectrum microscopy. Cell 158, 822–832.

Hanes RDL, Dalle-Ferrier C, Schmiedeberg M, Jenkins MC, Egelhaaf SU (2012). Colloids in one dimensional random energy landscapes. Soft Matter 8, 2714–2723.

He W (2015). Single-Particle Tracking of Acetylcholine Receptors and Ganglioside GM1 on Live Cell Membranes. PhD Thesis, Hong Kong University of Science and Technology.

He W, Song H, Su Y, Geng L, Ackerson BJ, Peng HB, Tong P (2016). Dynamic heterogeneity and non-Gaussian statistics for acetylcholine receptors on live cell membrane. Nat Commun 7, 11701.

Hoffman BD, Massiera G, Van Citters KM, Crocker JC (2006). The consensus mechanics of cultured mammalian cells. Proc Natl Acad Sci 103, 10259.

Höfling F, Franosch T (2013). Anomalous transport in the crowded world of biological cells. Rep Prog Phys 76, 046602.

Hunter GL, Weeks ER (2012). The physics of the colloidal glass transition. Rep Prog Phys 75, 066501.

Jacobson K, Liu P, Lagerholm BC (2019). The lateral organization and mobility of plasma membrane components. Cell 177, 806–819.

Jacobson K, Sheets ED, Simson R (1995). Revisiting the fluid mosaic model of membranes. Science 268, 1441.

Jung Hwan H, Yong-Hoon K, Jung-Ran N, Dong-Hee C, Kyoung-Shim K, AND CHUL-HO, L., LT, SUP, GT, LT, SUP & GT (2015). Enhanced

Production of adenosine triphosphate by pharmacological activation of adenosine monophosphate-activated protein kinase ameliorates acetaminophen-induced liver injury. Mol Cells 38, 843–850.
Kraft ML (2013). Plasma membrane organization and function: moving past lipid rafts. Mol Biol Cell, 24, 2765–2768.
Kumar R, Saha S, Sinha B (2019). Cell spread area and traction forces determine myosin-II-based cortex thickness regulation. Biochim Biophys Acta Mol Cell Res 1866, 118516.
Kusumi A, Fujiwara TK, Chadda R, Xie M, Tsunoyama TA, Kalay Z, Kasai RS, Suzuki KGN (2012). Dynamic organizing principles of the plasma membrane that regulate signal transduction: commemorating the fortieth anniversary of Singer and Nicolson's fluid–mosaic model. Annu Rev Cell Dev Biol 28, 215–250.
Kusumi A, Nakada C, Ritchie K, Murase K, Suzuki K, Murakoshi H, Kasai RS, Kondo J, Fujiwara T (2005). Paradigm shift of the plasma membrane concept from the two-dimensional continuum fluid to the partitioned fluid: high-speed single-molecule tracking of membrane molecules. Annu Rev Biophys Biomol Struct 34, 351–378.
Lee CW, Peng HB (2007). The function of mitochondria in presynaptic development at the neuromuscular junction. Mol Biol Cell 19, 150–158.
Lee CW, Zhang H, Geng L, Peng HB (2014). Crosslinking-induced endocytosis of acetylcholine receptors by quantum dots. PLoS One 9, e90187.
Leyssens A, Nowicky AV, Patterson L, Crompton M, Duchen MR (1996). The relationship between mitochondrial state, ATP hydrolysis, [Mg2+]i and [Ca2+]i studied in isolated rat cardiomyocytes. J Physiol 496, 111–128.
Lindstrom J, Einarson B (1979). Antigenic modulation and receptor loss in experimental autoimmune myasthenia gravis. Muscle Nerve 2, 173–179.
Lingwood D, Simons K (2010). Lipid rafts as a membrane-organizing principle. Science 327, 46.
Luo W, Yu C-H, Lieu ZZ, Allard J, Mogilner A, Sheetz MP, Bershadsky AD (2013). Analysis of the local organization and dynamics of cellular actin networks. J Cell Biol 202, 1057.
Mandel LJ, Doctor RB, Bacallao R (1994). ATP depletion: a novel method to study junctional properties in epithelial tissues. II. Internalization of Na+,K(+)-ATPase and E-cadherin. J Cell Sci 107, 3315.
Mascalchi P, Haanappel E, Carayon K, Mazères S, Salomé L (2012). Probing the influence of the particle in single particle tracking measurements of lipid diffusion. Soft Matter 8, 4462–4470.
Meroz Y, Sokolov IM (2015). A toolbox for determining subdiffusive mechanisms. Phys Rep 573, 1–29.
Merritt EA, Sarfaty S, Akker FVD, L'hoir C, Martial JA, Hol WGJ (1994). Crystal structure of cholera toxin B-pentamer bound to receptor GM1 pentasaccharide. Protein Sci 3, 166–175.
Michalet X, Berglund AJ (2012). Optimal diffusion coefficient estimation in single-particle tracking. Phys Rev E, 85, 061916.
Mohamed AS, Rivas-Plata KA, Kraas JR, Saleh SM, Swope SL (2001). Src-class kinases act within the agrin/MuSK pathway to regulate acetylcholine receptor phosphorylation, cytoskeletal anchoring, and clustering. J Neurosci 21, 3806.
Munro S (2003). Lipid rafts: elusive or illusive? Cell 115, 377–388.
Novikov DS, Fieremans E, Jensen JH, Helpern JA (2011). Random walks with barriers. Nat Phys, 7, 508–514.
Parry BR, Surovtsev IV, Cabeen MT, O'Hern CS, Dufresne ER, Jacobs-Wagner C (2014). The bacterial cytoplasm has glass-like properties and is fluidized by metabolic activity. Cell 156, 183–194.
Peng HB, Baker LP, Chen Q (1991). Tissue culture of *Xenopus* neurons and muscle cells as a model for studying synaptic induction. In: Methods in Cell Biology, eds. BK KAY and HB PENG, New York: Academic Press, 36, 511–526.
Pinaud F, Michalet X, Iyer G, Margeat E, Moore H-P, Weiss S (2009). Dynamic partitioning of a glycosyl-phosphatidylinositol-anchored protein in glycosphingolipid-rich microdomains imaged by single-quantum dot tracking. Traffic 10, 691–712.
Prahalad P, Calvo I, Waechter H, Matthews JB, Zuk A, Matlin KS (2004). Regulation of MDCK cell-substratum adhesion by RhoA and myosin light chain kinase after ATP depletion. Am J Physiol Cell Physiol 286, C693–C707.
Prost J, Jülicher F, Joanny JF (2015). Active gel physics. Nat Phys 11, 111.
Renner M, Choquet D, Triller A 2009a. Control of the postsynaptic membrane viscosity. J Neurosci 29, 2926.
Renner ML, Cognet L, Lounis B, Triller A, Choquet D 2009b. The excitatory postsynaptic density is a size exclusion diffusion environment. Neuropharmacology 56, 30–36.
Ritchie K, Shan X-Y, Kondo J, Iwasawa K, Fujiwara T, Kusumi A (2005). Detection of non-Brownian diffusion in the cell membrane in single molecule tracking. Biophys J 88, 2266–2277.
Sadegh S, Higgins JL, Mannion PC, Tamkun MM, Krapf D (2017). Plasma membrane is compartmentalized by a self-similar cortical actin meshwork. Phys Rev X, 7, 011031.
Saffman PG, Delbrück M (1975). Brownian motion in biological membranes. Proc Natl Acad Sci 72, 3111.
Saxton MJ (2007). A biological interpretation of transient anomalous subdiffusion. I. Qualitative model. Biophys J 92, 13.
Sezgin E, Levental I, Mayor S, Eggeling C (2017). The mystery of membrane organization: composition, regulation and roles of lipid rafts. Nat Rev Mol Cell Biol 18, 361–374.
Shi Z, Graber ZT, Baumgart T, Stone HA, Cohen AE (2018). Cell membranes resist flow. Cell 175, 1769–1779.e13.
Singer SJ, Nicolson GL (1972). The fluid mosaic model of the structure of cell membranes. Science 175, 720.
Smith PR, Morrison IEG, Wilson KM, Fernández N, Cherry RJ (1999). Anomalous diffusion of major histocompatibility complex class I molecules on HeLa cells determined by single particle tracking. Biophys J 76, 3331–3344.
Soula H, Care B, Beslon G, Berry H (2013). Anomalous versus slowed-down Brownian diffusion in the ligand-binding equilibrium. Biophys J 105, 2064– 2073.
Su Y (2017). Colloidal Diffusion over Complex Potential Landscapes: From Quasicrystalline and Random Potentials to Live Cell Membranes. PhD Thesis, Hong Kong University of Science and Technology.
Triller A, Choquet D (2008). New Concepts in synaptic biology derived from single-molecule imaging. Neuron 59, 359–374.
Van Citters KM, Hoffman BD, Massiera G, Crocker JC (2006). The role of F-actin and myosin in epithelial cell rheology. Biophys J 91, 3946–3956.
Weigel AV, Simon B, Tamkun MM, Krapf D (2011). Ergodic and nonergodic processes coexist in the plasma membrane as observed by single-molecule tracking. Proc Natl Acad Sci USA 108, 6438–6443.
Wong IY, Gardel ML, Reichman DR, Weeks ER, Valentine MT, Bausch AR, Weitz DA (2004). Anomalous diffusion probes microstructure dynamics of entangled F-actin networks. Phys Rev Lett 92, 178101.
Xu K, Babcock HP, Zhuang X (2012). Dual-objective STORM reveals three-dimensional filament organization in the actin cytoskeleton. Nat Methods 9, 185–188.
Zhang HL, Peng HB (2011). Mechanism of acetylcholine receptor cluster formation induced by DC electric field. PLoS One 6, e26805.